World Conference on Mechanical Engineering

Berlin, Germany 09-11 Dec 2022

Numerical Study of Nozzle Flow for a Rocket Engine Operating with Liquid Oxygen/Methane Propellants

Abderrahmane Zidane[1, *], Feriel Hasballaoui[1] and Mohamed Reda Abtouche[1]

[1] Thermal Energy Department, University of Science and Technology Houari Boumediene, Algeria

*Corresponding author

Abstract

The present work is an investigation of the reacting nozzle flow for a rocket engine using liquid oxygen and methane as propellants. The RL10A-3-3A rocket engine is selected as the baseline of this study, due to the availability of its nozzle profile. The simulations in this study were carried out using the commercial CFD software ANSYS Fluent. The first case is the simulation of the actual rocket engine nozzle flow with hydrogen. For this case, the reduced Evans and Schexnayder reaction model, with 6 species and 8 reactions, is used. Keeping the same chamber pressure, methane is then used as fuel instead of hydrogen for the second case. The third case is for a much higher chamber pressure using methane. A reduced model of the reaction mechanism for oxygen/methane combustion, with 8 species and reactions, is employed. A comparison of the obtained results for the three cases shows that the expansion of the hot gases produced in the combustion chamber through the nozzle is much more important for the hydrogen case compared to the methane case. Nonetheless, a much higher chamber pressure improves the hot gases expansion of the methane case. Finally, results show that liquid methane can be a viable replacement for hydrogen as a reusable rocket propellant.

Keywords: Reacting flow, Numerical Simulation, RL10A rocket engine.

1. Introduction

One of the major challenges that the aerospace community is currently attempting to overcome is manned space travel to Mars. This challenge includes a variety of aspects such as life support systems, radiation shielding, propulsion systems, and so on. The propulsion system required for this purpose must be both powerful and efficient, hence encouraging the development of higher-performing nozzles.

At the beginning of liquid rocket propulsion, a large number of propellant combinations were investigated in order to evaluate their potential for space propulsion, with various properties such as energy content, density, volatility, corrosivity, and reactivity used as criteria (Clark, 1972; Edwards, 2003; Morgan & Meinhardt, 1995). Analytical evaluations and experimental testing were used in these investigations (Cecere et al., 2014). Over 1800 fuels and approximately 2000 bi-propellant combinations were investigated, but only 40 different combinations flew at least once (Sutton, 2003).

The two most widely used combinations are liquid oxygen with hydrogen (LOX/ H_2) and liquid oxygen with kerosene (for example LOX/RP-1). This common use of these combinations led the development programs of heavy space transportation systems to concentrate on the development of numerical models for rocket engines using these propellant combinations (Schneider et al., 2018).

With the growing interest in reusable space transportation systems, the use of methane (CH_4) as the fuel for next-generation rocket engines is becoming more prominent. Thus, methane is considered the next-generation rocket propellant (Hagemann et al., 2016). This strong interest in methane applications in rocket propulsion (Battista et al., 2017; Deneuve A et al., 2017; Dutheil & Boué, 2017; Hahn et al., 2017; Iannetti et al., 2017; Liuzzi et al., 2017) is sprung from the possibility of developing low-cost space transportation systems for a variety of applications ranging from space tourism (Dutheil & Boué, 2017) to Mars missions (Bouyahiaoui et al., 2019, 2020). The cost-cutting offered by methane use stems from its unique properties, which include high energy value at low molecular weight combustion products, a small difference in temperature and density between methane and oxygen in liquid states, and acceptable coolant performance at low thermal loads on the liner (Hagemann et al., 2016).

Currently, rocket engine design is accomplished through the extensive use of numerical simulations. Accurate numerical simulations significantly reduce development costs by reducing the number of subscale, prototype, and test engines and their tests required (Knab et al., 2009, 2019). Several numerical studies have been conducted on rocket engine nozzle flows (Betelin et al., 2013, 2014; Kim, 1991; Smirnov et al., 2014; Zidane et al., 2019, 2021). These studies focused on rocket engines using the LOX/H_2 propellant combination.

On the other hand, a recent study focused on the development of a numerical model for the prediction and investigation of a dual-bell nozzle's transition behavior under LOX/CH_4 hot-flow conditions (Schneider et al., 2018). Therefore, a complex reaction mechanism (66-step) was implemented to the DLR-Tau solver and compared to a reduced seven-step model. The reduction of the chemical reaction mechanism results in a 93% reduction in computational cost. The numerical simulations achieved a good agreement with the experimentally obtained transition nozzle pressure ratio values. Another investigation concentrated on the impact of methane oxidation kinetics on a rocket nozzle flow (Zhukov, 2019). A comparison of the flow simulations between hydrogen/oxygen and methane/oxygen propellant combinations, and for three different reaction models: frozen flow, chemical nonequilibrium flow, and chemical equilibrium flow. The difference in results between chemical nonequilibrium and equilibrium flows is negligible for hydrogen but noticeable for methane.

The present study concentrates on the numerical investigation of a rocket nozzle flow using the LOX/CH_4 propellant combination. For comparison, the simulations of the nozzle flow are conducted for three cases: a hydrogen case (LOX/H_2), a low-pressure methane case (same pressure as the H_2 case), and a high-pressure methane case (much higher than the H_2 case). The main focus is the impact of the use of the oxygen/methane combination on the performance of an actual rocket engine, the RL10A-3-3A in this case.

2. Physical model and numerical method

Table 1: Summary of combustion chamber/nozzle characteristics.

Name	Symbol	Value
Combustion chamber radius	r_{cc}	0.1303 m
Throat radius	r_{th}	0.0627 m
Nozzle area ratio	A_e / A_{th}	61
Total nozzle length	L	1.476 m

Source: (Binder et al., 1997)

2.1 Physical model

The RL10A-3-3A rocket engine nozzle is the base of this study. This engine is a second-stage engine based on the expander cycle. Liquid hydrogen (LH2) is employed as fuel along with liquid oxygen as an oxidizer (LOX). The nozzle profile is taken from its manual (Binder et al., 1997). The summary of the nozzle geometrical parameters is listed in Tab. 1. Fig. 1 represents the nozzle geometry, the used mesh along with the used boundary conditions.

Figure 1: Nozzle geometry with fine mesh and used boundary conditions.

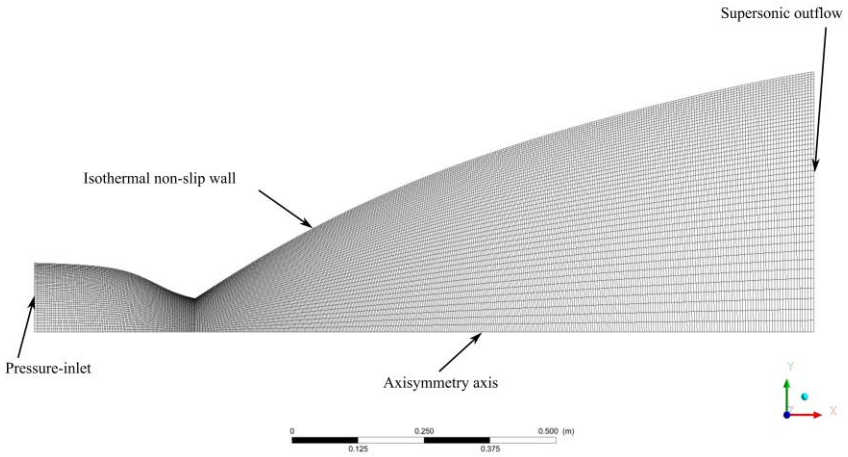

2.2 Numerical method

All cases in this study are solved by the commercial CFD software ANSYS Fluent 22. The steady-state density-based solver is employed to solve the axisymmetric two-dimensional Navier-Stokes equations for a laminar reacting flow. Inviscid flux vectors are discretized using the AUSM scheme. The least-square cell method is used to calculate gradients. The third-order MUSCL scheme is used for the flow equations, and an implicit scheme is employed for time stepping. Chemical reactions are modeled using the laminar finite rate reaction model and reaction rates are calculated using the Arrhenius formulation, as follows:

$$k_f = AT^b \exp\left(-E_a / RT\right) \tag{1}$$

where k_f is the forward reaction rate, A is the pre-exponential factor, T is the temperature, b is the temperature exponent, E_a is the activation energy, and R is the universal gas constant. The reverse reaction rates and third-body efficiencies are taken into consideration. The employed reaction mechanisms are discussed in the results section.

In order to impose a subsonic inlet condition, the *pressure-inlet* boundary condition is used, which is commonly used in nozzle flow simulations. Considering the fact that the flow is considered to be axisymmetric, an *axis* boundary condition is used. The *pressure-outlet* condition is applied for the supersonic outlet. The employed condition for the nozzle wall is non-slip along with an isothermal wall with a temperature $T_{wall} = 400K$.

Figure 2: Centerline Mach number profiles for different meshes.

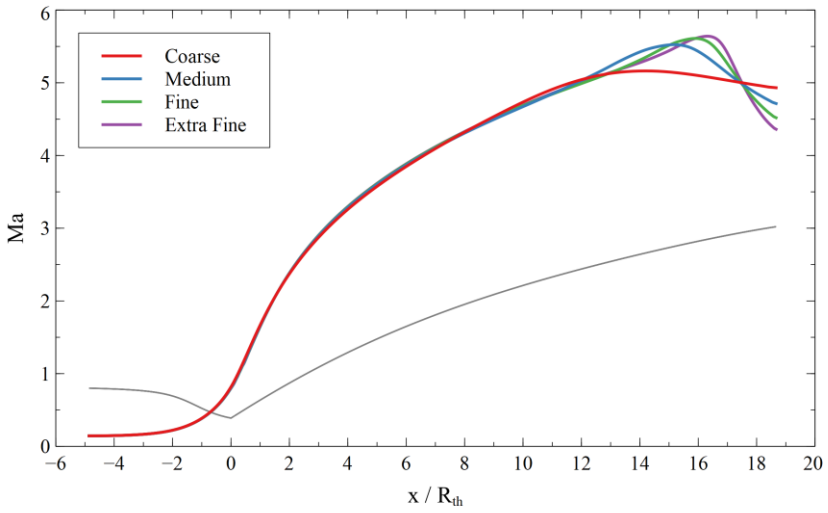

A structured mesh is used in this study. A mesh independence test is conducted in the nozzle for which hot gases are assimilated to water vapor in order to reduce computation time. Four different meshes are selected: coarse (2,400 elements), medium (9,600 elements), fine (21,600 elements), and extra fine (38,400). Fig. 2 shows the centerline Mach number profiles for these different meshes. The coarse mesh has the least number of elements, resulting in the least computation time. However, this mesh gives almost the same results as the rest but fails to capture the pressure wave effect on the centerline Mach number as seen in the $14 \leq x/r_{th} \leq 18.5$ region. The rest of the meshes capture this interaction with a difference in intensity. Moreover, the fine and extra fine mesh curves are mostly overlapped. In order to save computational efforts and improve accuracy, the fine mesh with 21,600 elements is adopted for the rest of the simulations.

3. Results and interpretations

All the simulated cases in this work are listed in Tab. 2. The first case is the simulation of the actual rocket engine operation; thus, hydrogen is used as fuel. Therefore, the reduced Evans and Schexnayder reaction mechanism (6 species and 8 reactions) is employed (Evans & Schexnayder, 1980).

For the second and third cases, hydrogen is substituted with methane as fuel. Hence, a reduced reaction mechanism with 8 species and 16 reactions is used (Schneider et al., 2018). The combustion chamber conditions, i.e., the mixture ratio O/F and pressure, for the hydrogen case are the actual engine conditions. For the second case, the low-pressure methane case, the chamber pressure is kept the same as the engine's operating pressure. However, the mixture ratio is 3.8, as used for the SpaceX Raptor engine. Regarding the third case, the high-pressure methane case, the mixture ratio is kept as for case 2, and the chamber pressure is 300 bar, the same as the Raptor engine.

Table 2: Summary of combustion chamber conditions for the different cases.

Case	1	2	3
Fuel	H_2	CH_4	CH_4
O/F	5.26	3.8	3.8
p_t $[bar]$	33.23	33.23	300
T_t $[K]$	3283.25	3463.56	3767.91

At the nozzle inlet, the *pressure-inlet* condition is applied by specifying the total pressure and temperature for each case. The combustion gases' residence time in the combustion chamber was assumed to be long enough to achieve chemical equilibrium. Thus, the flow is assumed to enter in a chemical equilibrium state (Schneider et al., 2018). Therefore, mixture composition at the nozzle's inlet is computed using the well-known NASA's Chemical Equilibrium with Application program using the conditions listed in Tab. 2.

Figure 3: Mach number distribution for the hydrogen case.

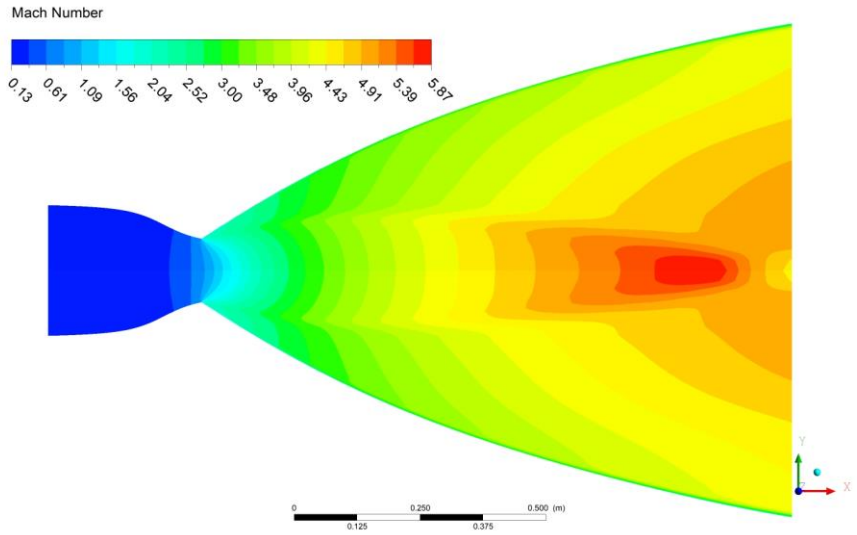

Fig. 3 illustrates the Mach number distribution through the nozzle for the hydrogen case. A classical nozzle gas expansion is observed, where a Mach number higher than 5.4 is reached at the nozzle's exit area. The influence of the pressure wave created by the hard edge in the throat can be clearly seen in the centerline near the exit. In this region, the highest value in Mach number, about 5.8, is reached.

Figure 4: Mach number distribution for the low-pressure methane case.

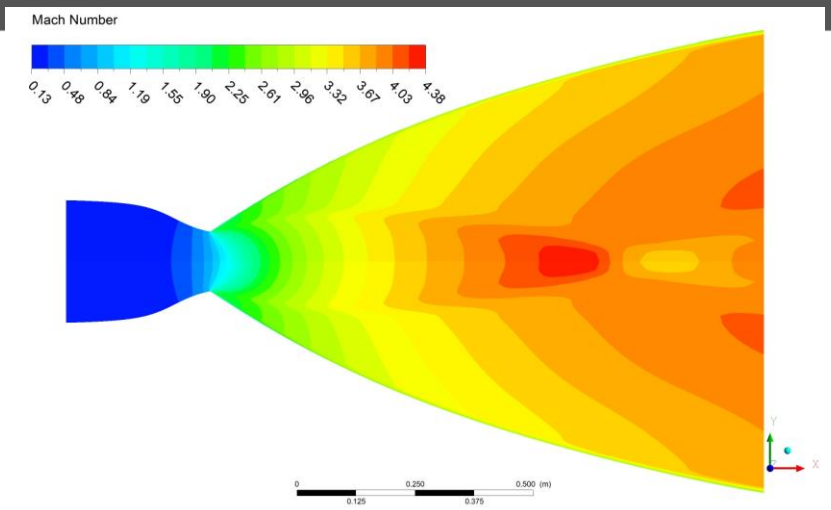

Figure 5: Mach number distribution for the high-pressure methane case.

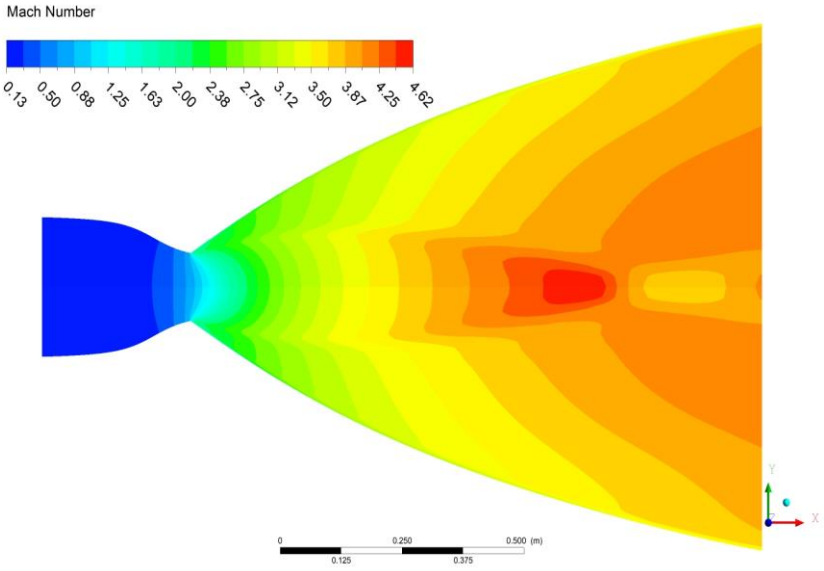

For the low and high-pressure methane cases (see Fig. 4 and 5), the same phenomena can be observed with a difference in Mach number value at the exit, where it is around 4.0 and 4.3, respectively. A comparison between the centerline Mach number profiles is illustrated in Fig. 6, where the previously noted difference in Mach numbers appears clearly. Fig. 7 – 9 represents the temperature distribution through the nozzle for the hydrogen, low-pressure, and high-pressure methane cases, respectively. In the convergent region, the temperature is almost constant and equal to the chamber temperature for all cases. Afterward, the temperature drops to less than 1000 K for the hydrogen case due to the expansion of the combustion gases.

Figure 6: Comparison of the centerline Mach number profiles between all cases.

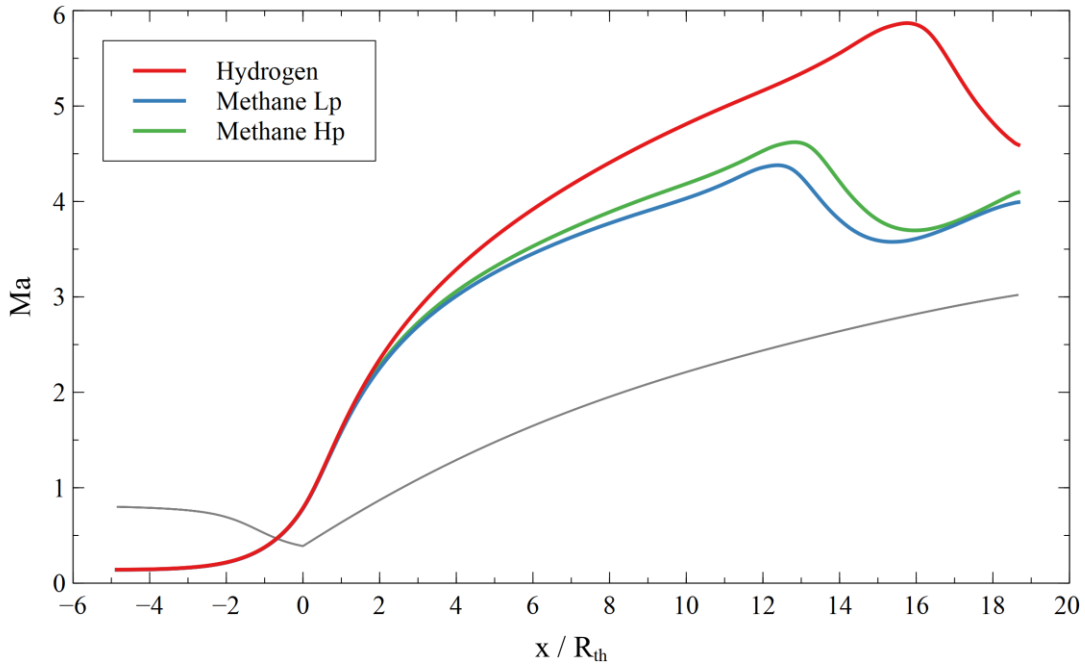

For the two methane cases, they present a similar temperature profile. The only noticeable difference is the temperature drop is less important than the first case, where it reaches a temperature around 1929 and 1801 K at the exit area for the low-pressure and high-pressure cases, respectively. This indicates that the methane gas mixture still holds much more internal energy, suggesting that it can be expanded even more. Thus, a nozzle with an even more important expansion ratio should be used.

The comparison in temperature ratio illustrated in Fig. 10 shows more clearly the difference in temperature drop due to the gases expansion. The temperature ratio for the methane cases is between 0.5 and 0.6, while it drops to the $0.2-0.3$ region for the hydrogen case. Another interesting result is that a higher chamber

pressure results in a better combustion gases expansion, where a higher Mach number and a lower temperature are reached for the high-pressure case compared to the low-pressure case.

Figure 7: Temperature distribution for the hydrogen case.

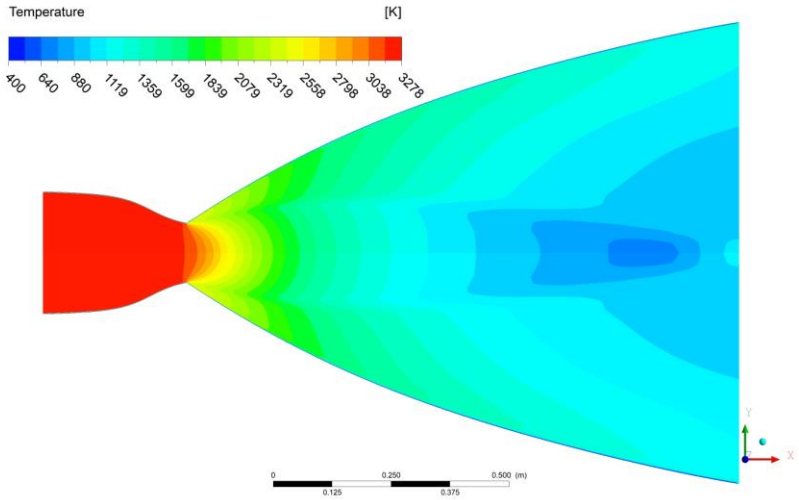

Figure 8: Temperature distribution for the low-pressure methane case.

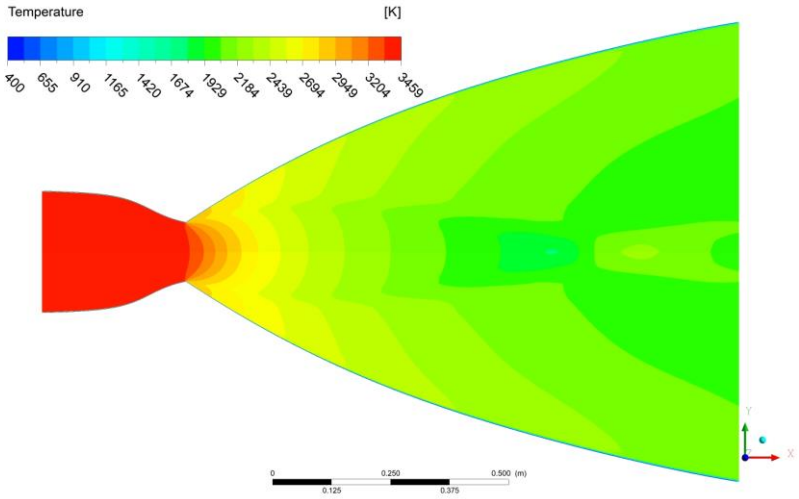

Figure 9: Temperature distribution for the low-pressure methane case.

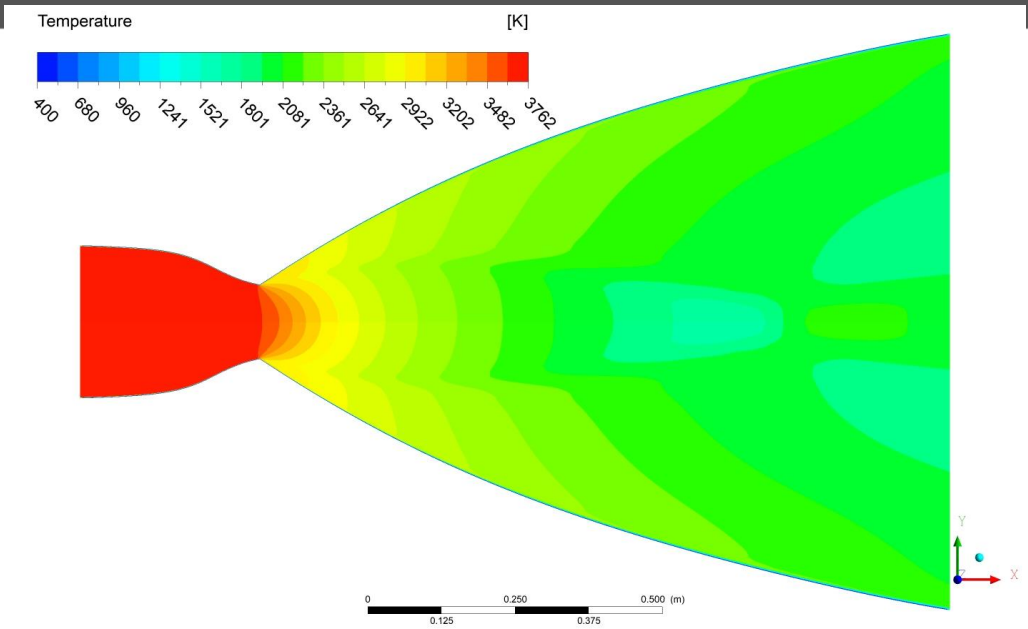

Figure 10: Comparison of the centerline temperature ratio profiles between all cases.

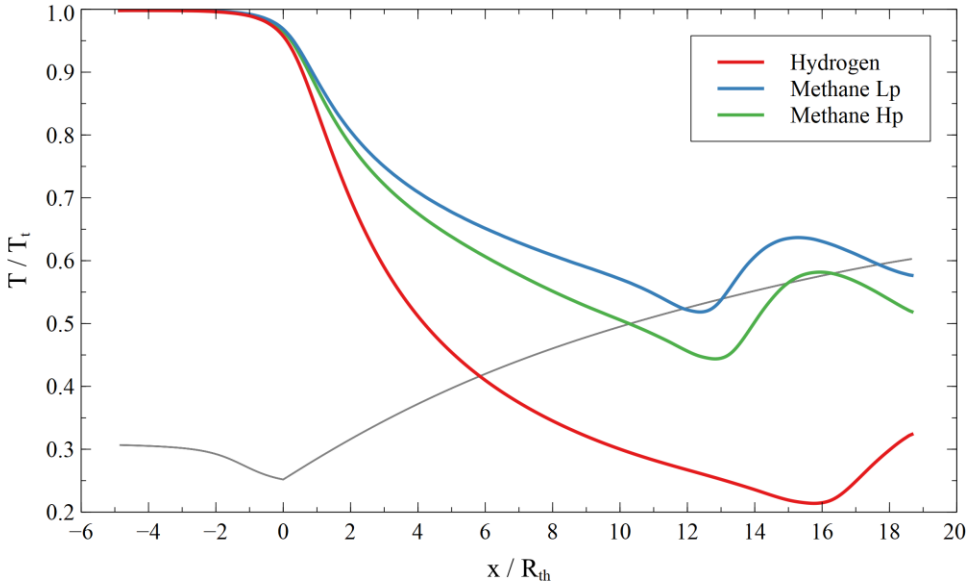

Figure 11: Centerline mass fraction profiles for the hydrogen case.

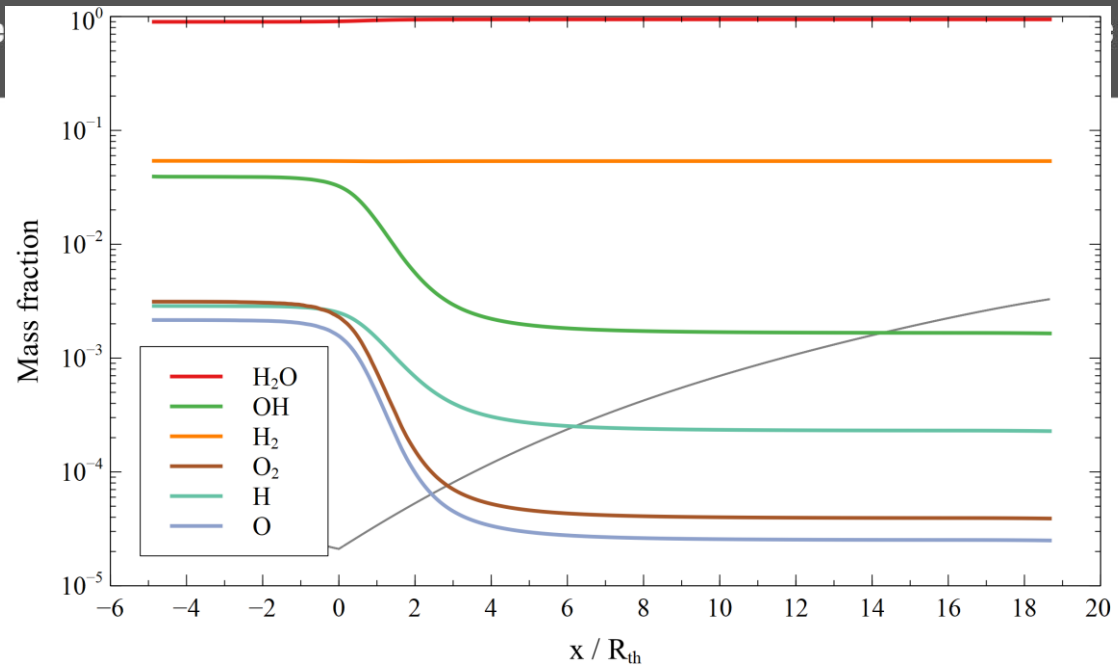

Figure 12: Centerline mass fraction profiles for the low-pressure methane case.

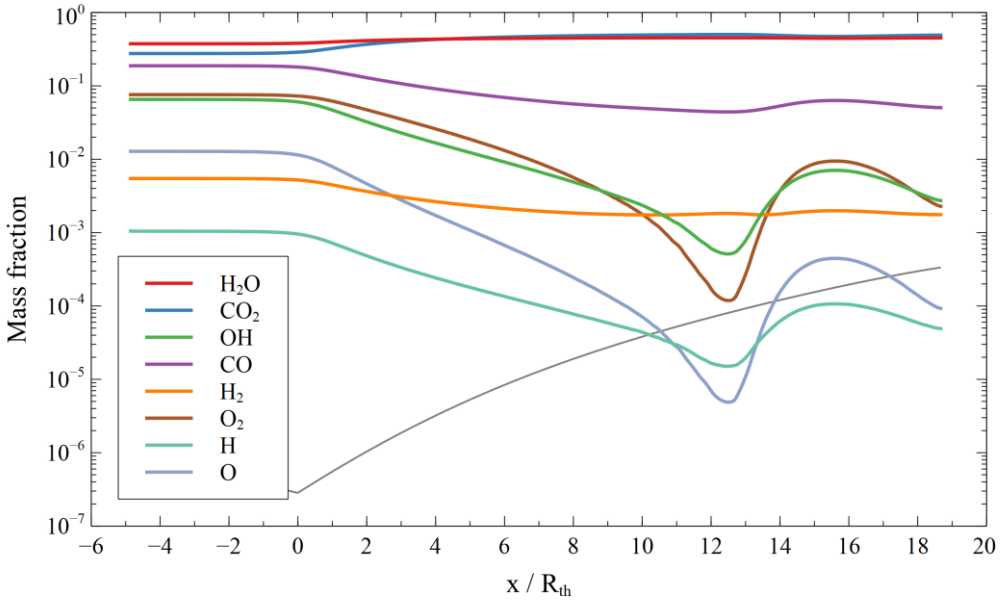

Figure 13: Centerline mass fraction profiles for the high-pressure methane case.

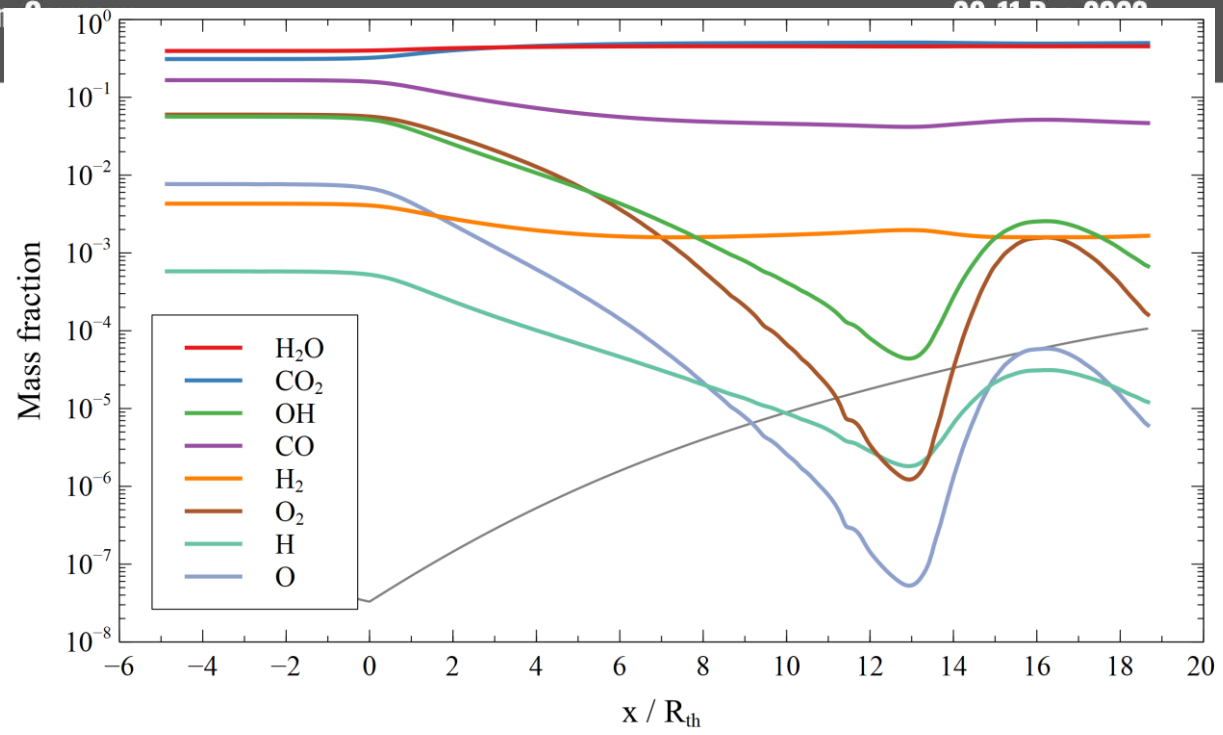

Figure 14: Comparison of the centerline mass fractions profiles for the methane cases: low-pressure (solid), high-pressure (dashed).

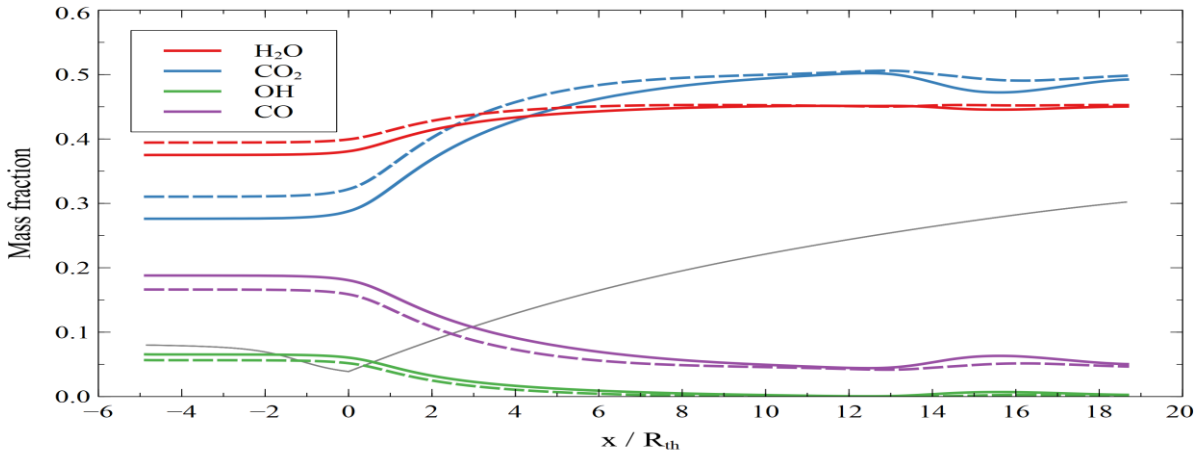

Figure 15: Comparison of the wall temperature ratio profiles between all cases.

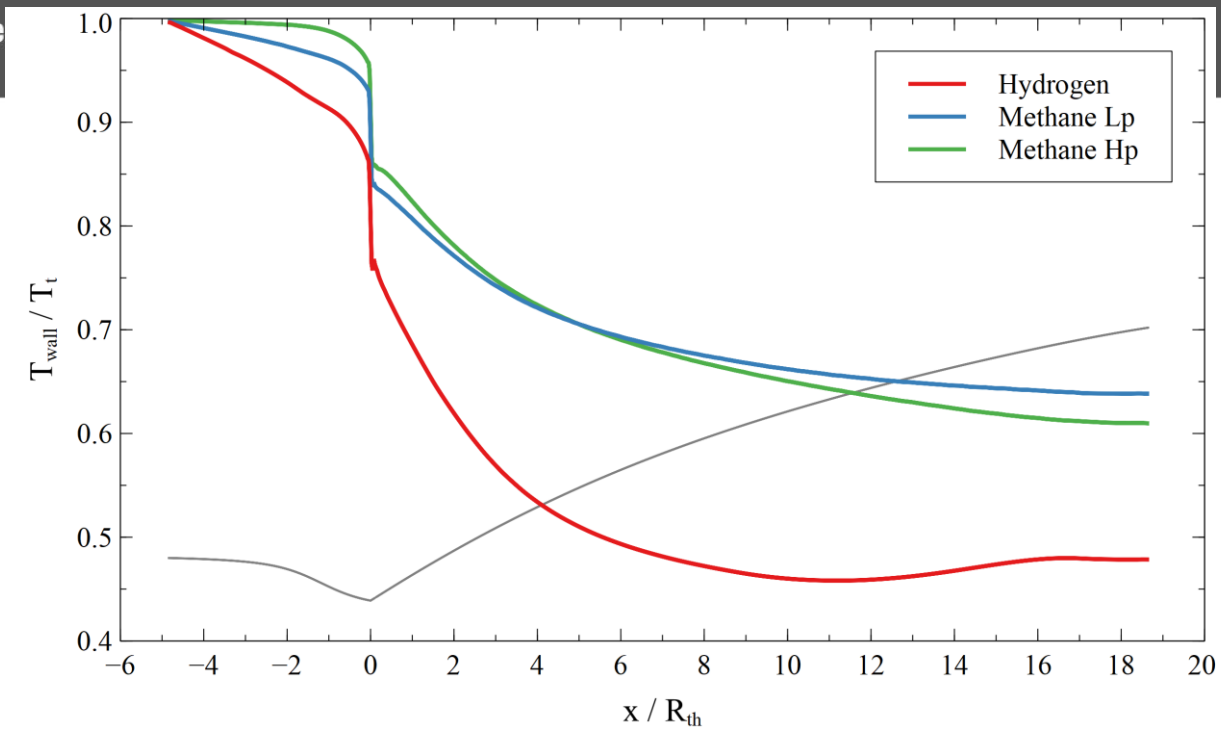

The mass fractions distributions along the nozzle centerline of the 6 species for the hydrogen are shown in Fig. 11. Only the water vapor slightly increases due to the recombination reactions occurring for the expansion flow conditions. Thus, the mass fraction of all other species decreases, except for the hydrogen (H_2) which seems to remain constant.

The same observations can be drawn for the methane cases illustrated in Fig. 12 and 13, where only water vapor and carbon dioxide mass fractions increase through the nozzle. The mass fraction of hydrogen can also be observed to be almost constant. A comparison of the mass fractions of the main products for the methane cases, i.e., water vapor H_2O, carbon dioxide CO_2, hydroxyl OH, and carbon monoxide CO, is shown in Fig. 14. The obvious observation that can be drawn is that the chamber pressure difference results in a slight variation in mass fraction values with the same global behavior. Fig. 15 represents the near-wall temperature to chamber temperature ratio through the nozzle. This near-wall temperature ratio also decreases with different rates through the nozzle. In the convergent region $x/r_{th} < 0$, the decrease rate for the hydrogen case is more important than for the methane cases. Moreover, the low-pressure case has a higher decrease rate than the high-pressure case. At the throat $x/r_{th} = 0$, a sudden drop in the near-wall temperature ratio is observed for all cases. This sudden drop is caused by the hard edge found at the throat.

Beyond the throat and in the $0 < x/r_{th} \leq 8$ region, the decrease rate is much more important than in the convergent. Beyond this region $x/r_{th} > 8$, the ratio is almost constant until the nozzle's exit. A high decrease in near-wall temperature ratio results in a high wall heat flux. In order to have an idea of the impact of using methane instead of hydrogen on the performance of the nozzle, the following parameters: mass flow, thrust, and specific impulse are computed at the nozzle's exit for all cases. The obtained results are listed in Tab. 3. Comparing the nozzle performance between the first and second cases, the main observation drawn from these results is that substituting hydrogen with methane results in a higher mass flow and thrust, but with a lower specific impulse. This is due to the fact that the molecular weight of the hot gases generated by methane combustion is higher than those obtained with hydrogen. Moreover, increasing chamber pressure results in an increase of the specific impulse as seen by comparing cases 2 and 3.

Table 3: Summary of computed nozzle performance for the different cases.

Case	1	2	3
Mass flow $\dot{m}$ $[kg/s]$	17.68	23.07	202.69
Thrust Th $[kN]$	78.85	83.23	745.85
Specific impulse I_{sp} $[s]$	454.69	367.93	375.23

4. Conclusion

In the present work, a numerical study of the reacting nozzle flow was carried out. Therefore, a reduced model of the reaction mechanism for LOX/CH_4 combustion is employed. The RL10A-3-3A rocket engine is selected as the baseline of this study. Three cases were simulated: the hydrogen case represents the actual rocket engine nozzle flow, the low-pressure methane case is the rocket nozzle flow using methane as fuel, and the high-pressure methane case is the same as the second but with a much higher chamber pressure. The obtained results showed that using methane instead of hydrogen with the same chamber pressure increases the mass flow, thus increasing the generated thrust at the nozzle's exit. However, this increase in mass flow and thrust comes at the expense of a decrease in specific impulse, therefore a decrease in nozzle performance. On the other hand, increasing the chamber pressure for the methane case increases the specific impulse and improves the performance. Finally, methane can be a viable replacement for hydrogen as a rocket propellant.

References

Battista, F., Ricci, D., Ferraiuolo, M., Cardillo, D., Fragiacomo, M., Natale, P., & Salvatore, V. (2017). The HYPROB LOX-LCH4 Demonstrator: status of the manufacturing and experimental activities. *7 TH EUROPEAN CONFERENCE FOR AERONAUTICS AND SPACE SCIENCES (EUCASS)*. https://doi.org/10.13009/EUCASS2017-360

Betelin, V. B., Nikitin, V. F., Altukhov, D. I., Dushin, V. R., & Koo, J. (2013). Supercomputer modeling of hydrogen combustion in rocket engines. *Acta Astronautica*, *89*, 46–59.

Betelin, V. B., Shagaliev, R. M., Aksenov, S. v, Belyakov, I. M., Deryuguin, Y. N., Korchazhkin, D. A., Kozelkov, A. S., Nikitin, V. F., Sarazov, A. v, & Zelenskiy, D. K. (2014). Mathematical simulation of hydrogen–oxygen combustion in rocket engines using LOGOS code. *Acta Astronautica*, *96*, 53–64.

Bouyahiaoui, Z., Haoui, R., Zidane, A., & Nouiri, A. (2019). Prediction of the flow field and convective heating during space capsule reentry using an open source solver. *International Journal of Heat and Mass Transfer*, *148*, 119045. https://doi.org/10.1016/j.ijheatmasstransfer.2019.119045

Bouyahiaoui Zineddine, Haoui Rabah, & Zidane Abderrahmane. (2020). Numerical investigation of a hypersonic flow around a capsule in CO2–N2 environment. *European Journal of Mechanics-B/Fluids*, *80*, 146–156.

Cecere, D., Giacomazzi, E., & Ingenito, A. (2014). A review on hydrogen industrial aerospace applications. *International Journal of Hydrogen Energy*, *39*(20), 10731–10747.

Clark, J. D. (1972). *Ignition!: An informal history of liquid rocket propellants*. Rutgers University Press.

Deneuve A, Humbert E, Lesaunier L, Dreyer S, Leudiere V, Herpe J, Theron M, du Tertre A, & Guichard D. (2017). BOREAS DEMONSTRATOR FOR FUTURE LIQUID PROPULSION ENGINES. *7 TH EUROPEAN CONFERENCE FOR AERONAUTICS AND SPACE SCIENCES (EUCASS)*. https://doi.org/10.13009/EUCASS2017-503

Dutheil, J.-P., & Boué, Y. (2017). Highly reusable LOx/LCH4 ACE rocket engine designed for SpacePlane: Technical Maturation progress via key system demonstrators results. *7 TH EUROPEAN CONFERENCE FOR AERONAUTICS AND SPACE SCIENCES (EUCASS)*. https://doi.org/10.13009/EUCASS2017-552

Edwards, T. (2003). Liquid fuels and propellants for aerospace propulsion: 1903-2003. *Journal of Propulsion and Power*, *19*(6), 1089–1107.

Evans, J. S., & Schexnayder, C. J. (1980). Influence of chemical kinetics and unmixedness on burning in supersonic hydrogen flames. *AIAA Journal*, *18*(2), 188–193.

Hagemann, G., Onofri, M., Schlechtriem, S., Wilson, F., & Rudnych, M. (2016). Plenary round table: LOX Methane. *Space Propulsion*.

Hahn, R. H. S., Waxenegger, G., Deeken, J., Oschwald, M., & Schlechtriem, S. (2017). Utilization of LOx/LCH4 for Expander-Bleed Cycle at Upper Stage Engine Application. *7 TH EUROPEAN CONFERENCE FOR AERONAUTICS AND SPACE SCIENCES (EUCASS)*. https://doi.org/10.13009/EUCASS2017-370

Iannetti, A., Girard, N., Tchou-kien, D., Bonhomme, C., Ravier, N., & Edeline, E. (2017). PROMETHEUS, A LOX/LCH4 REUSABLE ROCKET ENGINE. *7 TH EUROPEAN CONFERENCE FOR AERONAUTICS AND SPACE SCIENCES (EUCASS)*. https://doi.org/10.13009/EUCASS2017-537

Kim, S. (1991). Numerical study of high-area-ratio H2/O2 rocket nozzles. *27th Joint Propulsion Conference*, 2434.

Knab, O., Frey, M., Görgen, J., Quering, K., Wiedmann, D., & Mäding, C. (2009). Progress in combustion and heat transfer modelling in rocket thrust chamber applied engineering. *45th AIAA/ASME/SAE/ASEE Joint Propulsion Conference & Exhibit*, 5477.

Knab, O., Riedmann, H., Ivancic, B., Höglauer, C., Frey, M., & Aichner, T. (2019). Consequences of modeling demands on numerical rocket thrust chamber flow simulation tools. *Progress in Propulsion Physics–Volume 11*, *11*, 317–346.

Liuzzi Daniele, Rudnykh M, Drigo D, & Ierardo N. (2017). Architecture Trade-Off for the VEGA-E upper stage LOX/CH4 engine. *7 TH EUROPEAN CONFERENCE FOR AERONAUTICS AND SPACE SCIENCES (EUCASS)*. https://doi.org/10.13009/EUCASS2017-484

Morgan, O., & Meinhardt, D. (1995). Monopropellant selection criteria-hydrazine and other options. *35th Joint Propulsion Conference and Exhibit*, 2595.

Schneider, D., Génin, C., Stark, R., Oschwald, M., Karl, S., & Hannemann, V. (2018). Numerical model for nozzle flow application under liquid oxygen/methane hot-flow conditions. *Journal of Propulsion and Power*, *34*(1), 221–233. https://doi.org/10.2514/1.B36611

Smirnov, N. N., Betelin, V. B., Shagaliev, R. M., Nikitin, V. F., Belyakov, I. M., Deryuguin, Y. N., Aksenov, S. v, & Korchazhkin, D. A. (2014). Hydrogen fuel rocket engines simulation using LOGOS code. *International Journal of Hydrogen Energy*, *39*(20), 10748–10756.

Sutton, G. P. (2003). History of liquid propellant rocket engines in the United States. *Journal of Propulsion and Power*, *19*(6), 978–1007.

Zhukov, V. P. (2019). The impact of methane oxidation kinetics on a rocket nozzle flow. *Acta Astronautica*, *161*, 524–530. https://doi.org/10.1016/j.actaastro.2019.01.001

Zidane, A., Haoui, R., Sellam, M., & Bouyahiaoui, Z. (2019). Numerical study of a nonequilibrium H2- O2 rocket nozzle flow. *International Journal of Hydrogen Energy*, *44*(8), 4361–4373.

Zidane, A., Hasballaoui, F., & Tacine, Y. (2021). NUMERICAL STUDY OF SUPERSONIC COMBUSTION THROUGH A METHANE FUELED SCRAMJET. *6th INTERNATIONAL CONFERENCE ON ADVANCES IN MECHANICAL ENGINEERING ISTANBUL 2021 (ICAME 2021)*.